

## Elasticity of methane hydrate phases at high pressure

Jennifer Beam,<sup>1</sup> Jing Yang,<sup>1</sup> Jin Liu,<sup>1</sup> Chujie Liu,<sup>2</sup> and Jung-Fu Lin<sup>1,3,a)</sup>

<sup>1</sup>Department of Geological Sciences, Jackson School of Geosciences, The University of Texas at Austin, Austin, Texas 78712, USA

<sup>2</sup>Laboratory of Seismology and Physics of Earth's Interior, School of Earth and Space Sciences, University of Science and Technology of China, Hefei, Anhui 230026, China

<sup>3</sup>Center for High Pressure Science and Advanced Technology Research (HPSTAR), Shanghai 201203, China

(Received 18 January 2016; accepted 1 April 2016; published online 19 April 2016)

Determination of the full elastic constants ( $c_{ij}$ ) of methane hydrates (MHs) at extreme pressure-temperature environments is essential to our understanding of the elastic, thermodynamic, and mechanical properties of methane in MH reservoirs on Earth and icy satellites in the solar system. Here, we have investigated the elastic properties of single-crystal cubic MH-sI, hexagonal MH-II, and orthorhombic MH-III phases at high pressures in a diamond anvil cell. Brillouin light scattering measurements, together with complimentary equation of state (pressure-density) results from X-ray diffraction and methane site occupancies in MH from Raman spectroscopy, were used to derive elastic constants of MH-sI, MH-II, and MH-III phases at high pressures. Analysis of the elastic constants for MH-sI and MH-II showed intriguing similarities and differences between the phases' compressional wave velocity anisotropy and shear wave velocity anisotropy. Our results show that these high-pressure MH phases can exhibit distinct elastic, thermodynamic, and mechanical properties at relevant environments of their respective natural reservoirs. These results provide new insight into the determination of how much methane exists in MH reservoirs on Earth and on icy satellites elsewhere in the solar system and put constraints on the pressure and temperature conditions of their environment. *Published by AIP Publishing.* [<http://dx.doi.org/10.1063/1.4946795>]

### I. INTRODUCTION

Methane hydrates (MHs) are an important molecular solid that has captured a lot of research attention due to its potential as a future energy resource and for its role as a major greenhouse gas.<sup>1</sup> MH reservoirs are abundant on Earth and are commonly found in marine sediments such as in the Gulf of Mexico.<sup>1</sup> They are also believed to be major constituents of icy satellites, such as the moons of Saturn.<sup>2</sup> Therefore, it is of paramount interest to study their physics and chemistry at relevant pressure-temperature ( $P$ - $T$ ) environments in order to better understand their roles and implications in planetary and energy sciences.

Most clathrate hydrate phases consist of cages of water molecules, which are held in place and stabilized by van der Waals forces.<sup>3</sup> There are four pressure-induced primary structures of methane hydrates that have been identified and reported thus far: MH-sI, MH-sII, MH-II, and MH-III.<sup>4,5</sup> X-ray diffraction (XRD) and laser Raman spectroscopy have been used to identify the crystal structure of each phase.<sup>4-7</sup> Their derived equation of state (EoS) parameters and the unit cell parameters as a function of pressure have been calculated from X-ray and neutron diffraction.<sup>8,9</sup> The general chemistry of MH has been observed using Raman spectroscopy, and the intensity and the presence of different Raman peaks in the spectra give clues to the number of cages and the number of gas molecules in each cage.<sup>6,10,11</sup> MH-I consists of two

phases, MH-sI and MH-sII, which are both cubic.<sup>3,4</sup> Each unit cell of MH-sI has 2 different cage types: 2 small  $5^{12}$  cages and 6 medium  $5^{12}6^2$  cages, while MH-sII has 16 small  $5^{12}$  cages and 8 large  $5^{12}6^4$ , where, for example,  $5^{12}6^4$  is made up of 12 pentagons and 4 hexagons.<sup>3</sup> At around 0.9-1.0 GPa, MH-I transforms into the hexagonal MH-II. MH-II contains 3 small  $5^{12}$  cages, 2 small  $4^35^66^3$  cages, and 1 large  $5^{12}6^8$  cage.<sup>3,5,12</sup> At 1.9-2.0 GPa, MH-II then transits into MH-III, which is reported to be stable upwards of 42.0 GPa.<sup>5,13</sup> MH-III is not a caged clathrate, but an orthorhombic filled ice structure. This filled ice structure is a network of water molecules bound by hydrogen bonds, similar to that of ice-*Ih* that creates channel-like systems surrounding gas molecules.<sup>5</sup>

The crystal structures of MH-I and MH-III have been well established, whereas the process of identifying and naming the different phases and their respective structures has been a tumultuous road for the second main phase MH-II.<sup>3-7</sup> Loveday *et al.*<sup>8</sup> proposed that there are actually two separate MH-II structures, MH-sH which is hexagonal and MH-II which is hexagonal-like, because they found that MH-II fit to the MH-sH structure gives an absurd nearest-neighbor distance between oxygens. Loveday *et al.*<sup>5</sup> and Kumazaki *et al.*<sup>10</sup> confirmed that the MH-II and MH-sH structures are indeed the same; however, the naming and distinction of the hexagonal structure has continued to be un-unified and leads to much confusion in the field. In more recent papers, there is continued reference to the hexagonal structure as both MH-sH such as in Shu *et al.*<sup>14</sup> and MH-II such as in Huo *et al.*<sup>15</sup> This leads to a lot of confusion when simultaneously gathering information from older papers where MH-sH and MH-II were

a) Author to whom correspondence should be addressed. Electronic mail: [afu@jsg.utexas.edu](mailto:afu@jsg.utexas.edu).

believed to be two separate structures. We propose that a single name for the secondary major phase of clathrates be used, and in this paper, we confirm its structure and denote it as hexagonal MH-II.

It is of the utmost importance to understand the full elastic constants of the single-crystal MH phases at extreme P-T, because the elasticity provides a full description of their mechanical and elastic properties such as the bulk and shear moduli, the aggregate compressional and shear velocities, and the seismic anisotropies.<sup>12,15</sup> The elastic constants at high pressures also give clues into the thermodynamic stability of MH at high pressures. All three elastic constants for the cubic MH-sI phase have been reported experimentally at pressures up to 0.9 GPa through Brillouin light scattering experiments, while elastic constants of the hexagonal MH-II phase have been calculated theoretically.<sup>12,15</sup> Thus far, there has yet to be any published results of experimentally resolved elastic constants for the hexagonal MH-II and orthorhombic MH-III phases, and there are no reported elastic constants for the cubic MH-I at pressures above 0.9 GPa. Therefore, it is essential to study the elasticity of the single-crystal MH phases at higher pressures in order to decipher each phase's elastic and mechanical properties.

In this paper, we have investigated the elastic, vibrational, and compressional behaviors of single-crystal MH-I, MH-II, and MH-III phases at high pressures using complimentary Raman spectroscopy, X-ray diffraction, and Brillouin Light Scattering techniques in a diamond anvil cell (DAC). Raman spectroscopy and X-ray diffraction are used to identify the phase transformations at elevated pressures as well as to investigate the cage occupancy and the chemistry. Experimentally measured Brillouin spectra are used to derive sound velocities and to evaluate elastic constants of all three phases, as well as the aggregate velocities, the bulk and shear moduli, and the compressional and shear wave anisotropies for MH-sI and MH-II. These results are used to evaluate the thermodynamics and elastic properties of single-crystal

MH phases as a function of pressure and therefore their implications in terrestrial and non-terrestrial environments. These properties provide new insight into how to detect MH reservoirs and the amount of methane within them.

## II. EXPERIMENTS

The MH-I single crystals in this study were produced in a DAC with a pair of diamond anvils having 750  $\mu\text{m}$  culets. Following the procedure of Shimizu *et al.*, the crystals were synthesized in the sample chamber of the DAC made of a Re gasket with an initial thickness of 250  $\mu\text{m}$  that was pre-indented to a thickness of approximately 30  $\mu\text{m}$  and then a 300  $\mu\text{m}$  wide hole was drilled.<sup>12</sup> A thin sample chamber was necessary in order to ensure that the as-grown MH crystals would be touching both culets so that the wave vector of the acoustic phonons would remain parallel to the diamond cutlet faces.<sup>12</sup> This also helps to avoid unwanted signals from water and ice when taking Brillouin and Raman measurements. Distilled water was sealed into the sample chamber, together with a few ruby spheres as the pressure calibrant. A small amount of water was then released to create a bubble of air whose size was based on the over-estimation for synthesizing MH-sI methane clathrates with 5.75:1 mole ratio between water and  $\text{CH}_4$  at ambient conditions resulting in a volume ratio of 1:1 (Fig. 1(a)). Consequently, methane gas (99.9995% purity from Air Gas) was compressed to 20 000 PSI and loaded into the sample chamber have had water and an air bubble using the Gas-Loading System at the Mineral Physics Laboratory of the University of Texas at Austin. The DAC was then tightened to  $\sim 0.2$  GPa and the mixture of  $\text{CH}_4$  and  $\text{H}_2\text{O}$  was allowed to stabilize over the course of several days. The first visual evidence of clathrates was observed via an optical microscope immediately after loading at 0.1 GPa and ambient temperature; small, needle-like crystals were scattered across the sample chamber. Pressure was measured and monitored

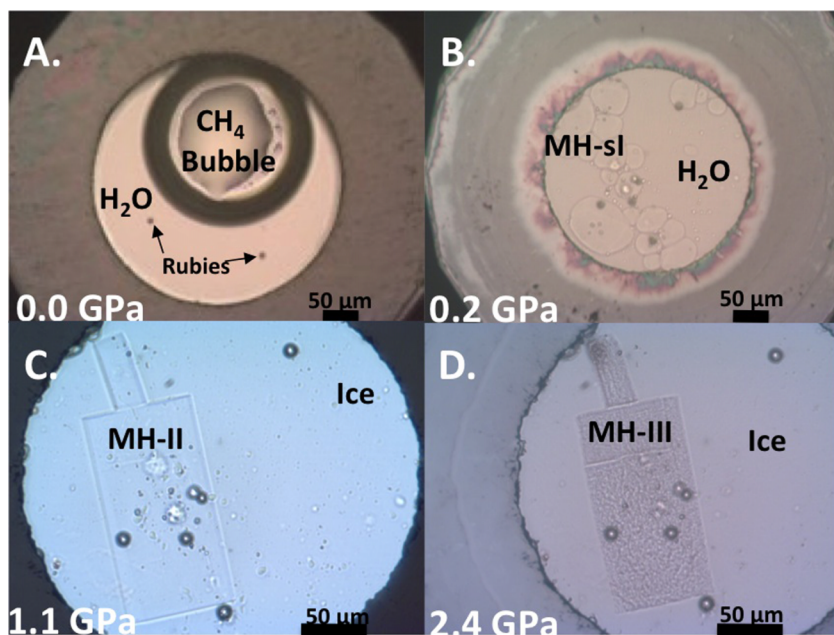


FIG. 1. Photographs of the synthesis of methane clathrate crystals in a DAC chamber at representative pressures and ambient temperature. (a) Starting sample chamber with a methane gas bubble, water, and ruby spheres at ambient conditions, (b) cubic MH-sI phase at 0.2 GPa, (c) hexagonal MH-II phase at 1.1 GPa, and (d) orthorhombic MH-III phase at 2.4 GPa.

using ruby as a pressure calibrant; four ruby spheres were placed in the sample chamber and pressures determined from measured fluorescence spectra were averaged for each given pressure step. Pressure uncertainties were calculated based on the standard deviations from multiple fluorescence spectra of the ruby spheres before and after the experiments at each pressure step.<sup>16</sup> In order to grow larger crystals, the temperature was cyclically increased to just below the melting temperature, approximately 50 °C, and then, decreased back to ambient conditions numerous times.<sup>10</sup> However, the process in cycling the temperature did not significantly cause the crystals to re-nucleate and grow effectively, so the pressure of the cell was cycled slowly until larger crystals formed and stabilized (Fig. 1(b)). The pressure was decreased by ~0.05 GPa and allowed to stabilize for ~15 min, then the pressure was increased back to the initial pressure. This procedure proved to be much more effective at lower pressures and was repeated until the crystals reached a formidable size. The largest crystal formed was approximately 80  $\mu\text{m}$  across and 70  $\mu\text{m}$  wide. The pressure was then incrementally increased in order to reach and complete each phase transition while temperature was held constant at 298 K. The phase transition to MH-II occurred at 0.93 GPa, where 2 large crystals formed (Fig. 1(c)). The largest crystal was 150  $\mu\text{m}$  across and 75  $\mu\text{m}$  wide, while the smaller crystal was approximately 60  $\mu\text{m}$  across and 20  $\mu\text{m}$  wide. MH-III was reached and stabilized at 2.00 GPa (Fig. 1(d)). The crystal shapes remained constant during and after the phase transition from MH-II to MH-III. The MH-III crystals became opaque as pressure was increased above 2.70 GPa, most likely due to forming polycrystalline. The opaqueness prevented a Brillouin signal from being seen; therefore, the procedure from Kumazki *et al.*<sup>10</sup> was followed, where the crystal was heated above the dissociation temperature, ~453 K, in order to regrow single MH-III crystals. The sample stabilized at 2.70 GPa, and numerous smaller MH-III crystals formed. At this higher pressure cycling, the pressure was less effective than cycling the temperature, so the temperature was cycled right below the dissociation temperature in order to nucleate and grow larger crystals.

The Raman system in the Mineral Physics Laboratory was used for the identification of MH phases at high pressures. The system was equipped with a Coherent Verdi V2 laser with a 532 nm wavelength, an electron multiplying charge-coupled device (EMCCD), and a Shamrock spectrometer from Andor Technology. The laser power was limited to ~2 mW to avoid overheating of the sample. Each Raman spectrum was collected with an exposure time of ~20 min to ensure quality data analyses in order to identify the MH phases and to observe the changes in the chemistry. Additionally, micro-Raman spectra were taken with the Witec Alpha 300 micro-Raman confocal microscope with a 488 nm laser and 1  $\mu\text{m}$  spatial resolution from the MH-II phase at 1.10 and 1.44 GPa in order to establish that the chemical composition of each given crystal was homogeneous.<sup>17</sup> The homogeneity was confirmed via analysis of the intensity ratios and the Full Width at Half Maximum (FWHM) of the Raman bands, which were shown to be consistent throughout the crystal.

High-pressure Brillouin measurements were conducted on the synthesized single crystal of each MH phase in the

Mineral Physics Laboratory of the University of Texas at Austin. The Brillouin system was equipped with a Coherent Verdi V2 laser with a wavelength of 532 nm, an APD detector (Count-10B Photo Counting Module from Laser Components, Inc.), and a JRS six-pass tandem Fabry–Pérot interferometer. The laser beam was focused down to approximately 20  $\mu\text{m}$  in diameter at the sample position. The scattered Brillouin signals were collected at a scattering angle of 46.8°, which was calibrated using a standard silica glass, distilled water, and single crystal MgO.<sup>18</sup> Brillouin light scattering measurements were performed at a pressure increment of approximately 0.2 GPa for each phase over a range of azimuthal angles at each pressure. Polarization and power of the incident laser were adjusted in order to reach the maximum signal-to-noise ratio from the single crystal for each phase.

High-pressure XRD experiments were performed on a second DAC with MH phases that were prepared similarly to the conditions for the first sample described above. These experiments were conducted up to approximately 5 GPa at the 13IDD beamline of the GSECARS of the Advanced Photon Source (APS), Argonne National Laboratory (ANL). A monochromatic X-ray beam with a wavelength of 0.3344 Å was focused down to ~3  $\mu\text{m}$  in diameter (FWHM) at the sample position. Diffraction patterns of the sample were collected by a MAR CCD and then integrated using Fit2D software. During each measurement, the DAC was rotated  $\pm 10^\circ$  about the vertical axis of the cell holder to allow sampling different orientations of the single-crystal phases. Pressures and their uncertainties were calculated from the multiple measurements from ruby spheres before and after the XRD measurements using an online ruby system.

### III. RESULTS

#### A. Raman spectroscopy results

The Raman spectra taken for MH-sI, MH-II, and MH-III phases as a function of pressure show that vibrational bands present in each spectrum correspond to the C–H stretching modes of the methane molecules in their water lattices (Fig. 2). The number of Raman bands, the frequency shifts, and the relative intensity of the bands were determined by the structure and chemistry of the cage types in each phase. Therefore, analysis of these bands can be used to identify the phase and to provide information regarding their chemistry (the number of methane molecules present in the cages). MH-sI has two peaks, where the first peak and second peak correspond to the medium  $5^{12}6^2$  cages and small  $5^{12}$  cages, respectively.<sup>7,10,19</sup> When the MH-sI transitioned to the hexagonal MH-II, one broad Raman band appeared which is the overlapping of the 3 types of cages: the small  $5^{12}$ , the small  $4^35^66^3$ , and the large  $5^{12}6^8$  in the phase (Figs. 2 and 3).<sup>7,10,19</sup> As pressure increased from 1.20 GPa to 1.44 GPa, the Raman band of the MH-II phase de-convolved into two separate Raman bands where the first band is the overlapping of the two small cage types and the second band is the large cages (Fig. 2).<sup>10</sup> The phase transition from MH-II to MH-III results in a single band, which is the result of the phase transformation to a filled ice structure where there are no cages (Fig. 2).<sup>7,10</sup>

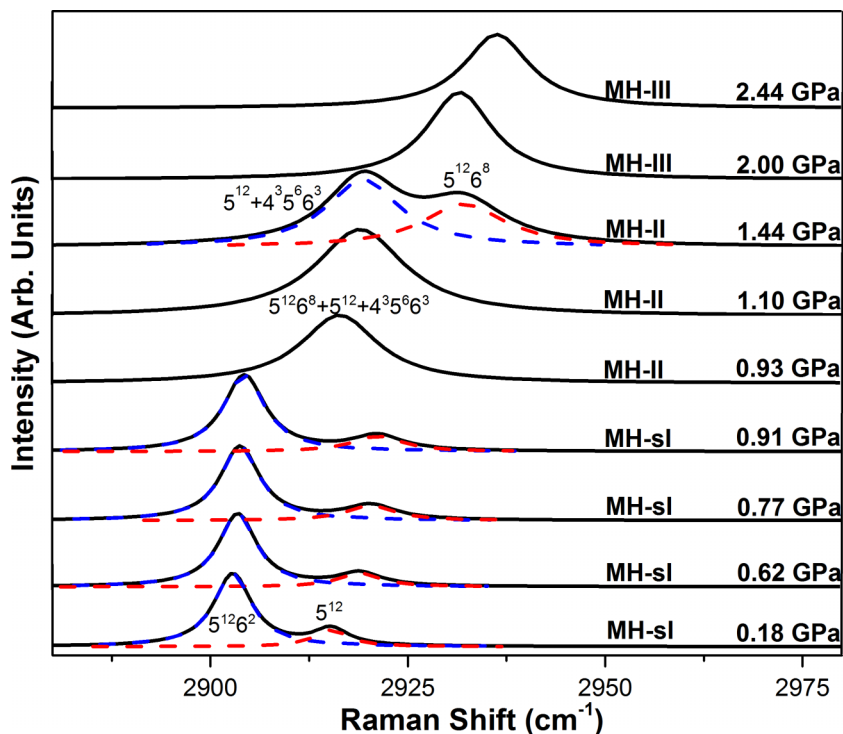


FIG. 2. Stacked high-pressure Raman spectra for C-H stretching modes of encaged methane molecules in MH-sI, MH-II, and MH-III phases at ambient temperature. At pressures from 0.18 to 0.91 GPa, Raman peaks for the large and small cages are present in MH-sI phase. Three cage types form a single peak in MH-II phase from 0.93 GPa to 1.10 GPa, which separates into two peaks as pressure increases (shown in the spectrum at 1.44 GPa). A single peak is present for MH-III phase starting at 2 GPa.

## B. X-ray diffraction results

XRD spectra were collected from MH-sI, MH-II, and MH-III phases as a function of increasing pressure up to approximately 5 GPa (Fig. 4). Previously reported Miller indices for MH-sI and MH-II phases from Shu *et al.*<sup>14</sup> and Harai *et al.*,<sup>13</sup> respectively, were used to index the  $d$ -spacings of our corresponding phases and to determine their lattice unit cell parameters. Diffraction peaks of the MH-III phase were identified based on the orthorhombic structural model

from Boulfif and Louer.<sup>20</sup> The  $d$ -spacings of the diffraction peaks and their identified Miller indices were then used to calculate the unit cell parameters and thus the volume for MH-sI and MH-II phases at each given pressure (Figs. 4 and 5). The  $d$ -spacings of the diffraction peaks, their respective Miller indices, and unit cell parameters for MH-III were calculated using the program dicvol06 (Figs. 4 and 5).<sup>20</sup> The mean molecular volume was then plotted as a function of pressure, which was fitted using the 3rd Birch-Murnaghan EoS (Fig. 5).<sup>21</sup> The volume of each phase has a negative

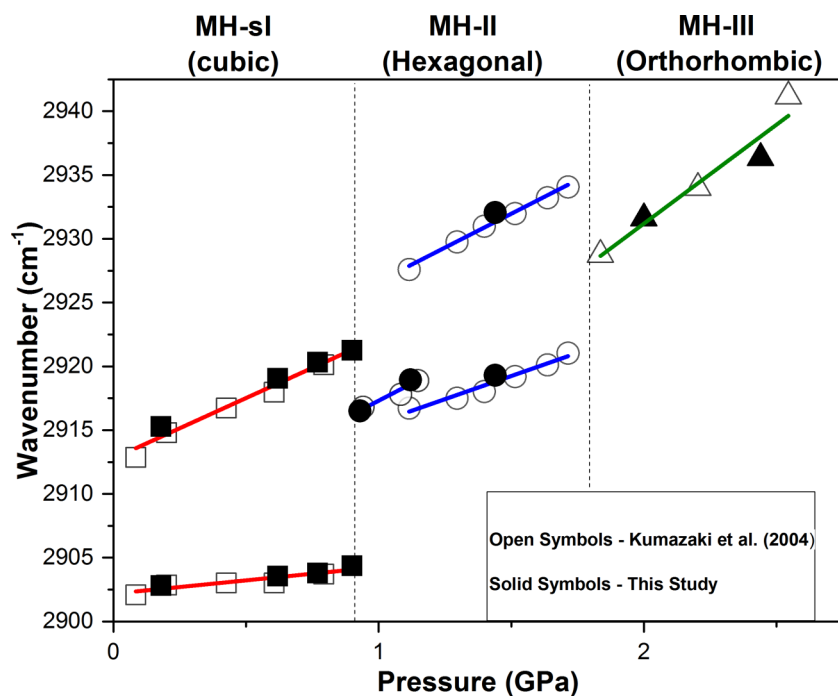


FIG. 3. Raman frequency shifts of C-H stretching modes of the caged methane molecules in MH-sI, MH-II, and MH-III phases as a function of pressure at ambient temperature. For MH-II phase, a single Raman mode splits into two modes starting at 1.44 GPa. Solid symbols are frequency shifts from this study. Open symbols are reported Raman shifts from Kumazaki *et al.*<sup>10</sup>

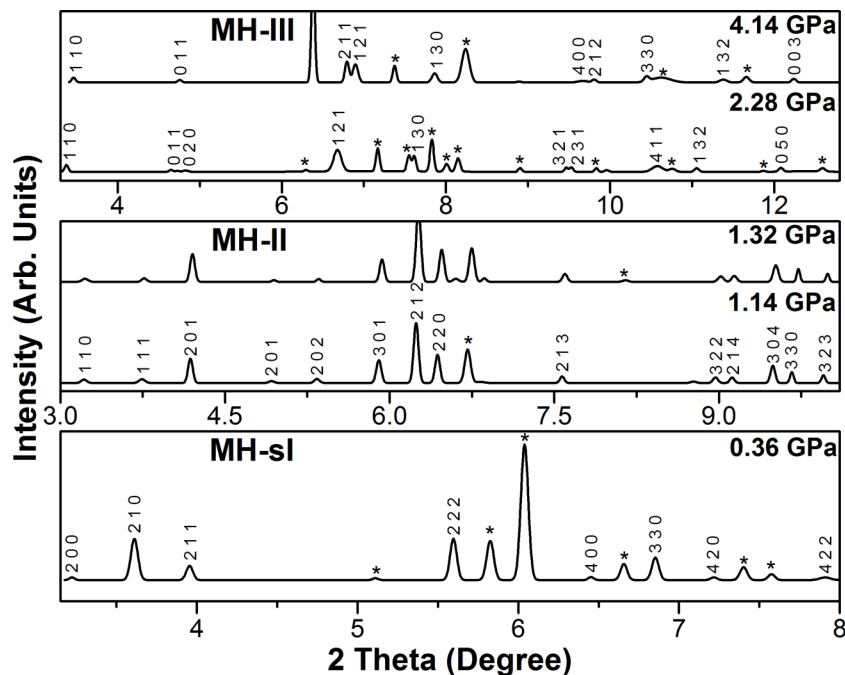


FIG. 4. Representative X-ray diffraction spectra of MH-sI, MH-II, and MH-III phases as a function of pressure at room temperature. Identified XRD peaks are labeled with their corresponding Miller indices. Diffraction peaks for MH-sI and MH-II phases were indexed with their respective Miller indices based on literature reports.<sup>13,14</sup> Miller indices for MH-III phase are based on the orthorhombic structural model reported by Boulfif *et al.*<sup>20</sup> (See Fig. 5 for further pressure-volume curve.) Asterisks indicate unidentified peaks.

correlation with pressure, and there is a volume drop across each phase transition. The transition from MH-sI to MH-II results in a volume decrease of 7.3%, while the transition from MH-II to MH-III is subtler with a volume decrease of 2.1% (Fig. 5). Then, the EoS parameters for each phase were used, along with estimated chemistry information from previous reports, in order to calculate more accurate densities at each pressure, which, together with Brillouin results discussed below, allowed for more accurate derivations of the elastic constants at high pressures.

### C. Brillouin light scattering results

Representative spectra for each phase and acoustic velocities are shown (Fig. 6) where the peaks from the longitudinal acoustic (LA) and transverse acoustic (TA) modes were identified when present. One compressional velocity ( $V_P$ ) and one shear velocity ( $V_S$ ) could be reliably identified for the single-crystal MH-sI phase at each pressure. Similarly,  $V_P$  and  $V_S$  peaks were identified for the hexagonal phase at 0.93 GPa and 1.44 GPa, but the  $V_S$  could not be

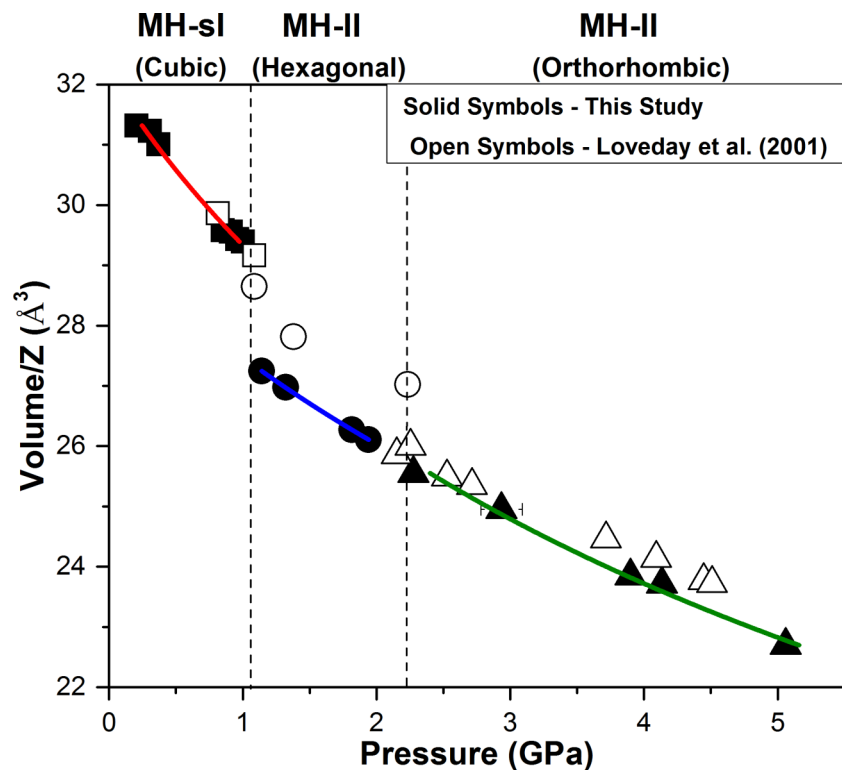


FIG. 5. Mean molecular volume of MH-sI, MH-II, and MH-III phases as a function of pressure at ambient temperature. Solid symbols are data from this study. Open symbols are data from Loveday *et al.*<sup>8</sup> Error bars are not shown when smaller than the symbols.

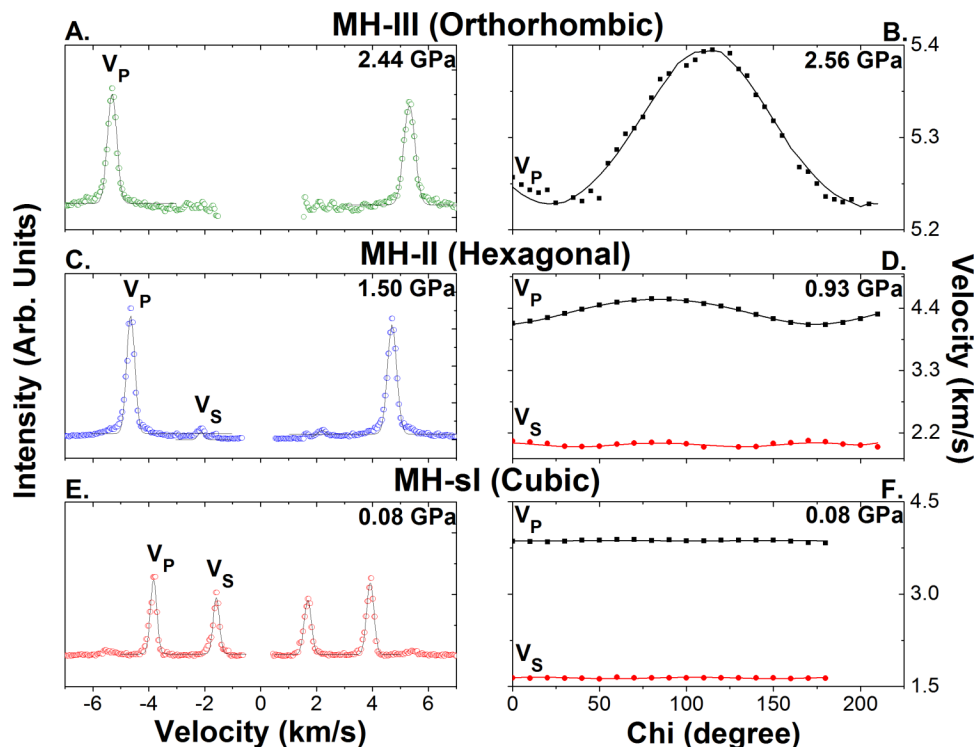


FIG. 6. Representative Brillouin light scattering spectra with compressional ( $V_P$ ) and shear velocity ( $V_S$ ) peaks (when present) for (a) MH-sI at 0.08 GPa, (b) MH-II at 1.50 GPa, and (c) MH-III at 2.44 GPa. Fitted  $V_P$  and  $V_S$  velocities as a function of the azimuthal angle for (d) MH-sI at 0.08 GPa, (e) MH-II at 0.93 GPa, and (f) MH-III at 2.56 GPa.

distinguished for the hexagonal phase at 1.20 GPa. Wave propagation consists of three different propagation types: longitudinal or compressional and two shear waves with opposite polarizations.<sup>22</sup> However, in the Brillouin light scattering data, a single peak for the TA modes is present for the cubic and hexagonal phases. This is likely due to the close frequency of the two shear modes, the weak intensity of one of the peaks, or weak coupling of the incident laser to the phonon wave vector.<sup>12</sup> Only the  $V_P$  could be identified for the orthorhombic MH-III phase at 2.00 GPa, 2.44 GPa, and 2.56 GPa due to the very low signal to noise ratio. Upon further pressure increase above 2.70 GPa, MH-III became brownish in color and neither the LA or TA modes could be detected due to the crystal being too dark for the incident laser. The peaks from the TA mode for the MH-sI phase were exceptionally strong, but as pressure increased the signal intensity decreased (Fig. 6). The Brillouin signals from the TA mode for MH-II were much weaker compared to that in MH-sI and became undetectable in the MH-III phase. The peaks for the  $V_P$  and  $V_S$  velocities over a range of azimuthal angles at each pressure allowed for the angular dependence of each velocity to be observed. This angular dependence was used to calculate the elastic constants for each phase as a function of pressure using Christoffel's equations in the IGOR software program (Fig. 7).<sup>23</sup> The bulk and shear moduli, the bulk sound velocity ( $V_\Phi = (K/\rho)^{1/2}$ ), and the aggregate compressional velocity ( $V_P = [(K_S + (4/3)G)/\rho]^{1/2}$ ) and shear velocity ( $V_S = [G/\rho]^{1/2}$ ) were then calculated using the derived elastic constants and the EoS parameters (Fig. 8). The representative anisotropy patterns of  $V_P$  and  $V_S$  of the single-crystal MH-I and MH-II phases were then calculated using the petrophysical software Unicef Careware (Fig. 9).<sup>24</sup>

Three elastic constants required to explain the cubic structure were derived for the cubic MH-sI:  $c_{11}$ ,  $c_{12}$ , and,  $c_{44}$ .

The adiabatic bulk modulus ( $K_S$ ) is the ratio of the hydrostatic stress to the volumetric strain when pressure is changed while entropy is constant, and the shear modulus ( $G$ ) is the ratio of the shear stress to the shear strain. Both moduli were calculated from the derived elastic constants as a function of pressure using the Reuss-Voigt-Hill average.<sup>25</sup>

An iterative procedure was used to further obtain the finite strain parameters for individual and aggregate elastic moduli ( $K_S$  and  $G$ ) as well as densities at high pressure in order to calculate more accurate stiffnesses and other resulting properties. The pressure derivatives of the elastic moduli at 298 K were obtained by fitting the moduli at high pressure using the third-order Eulerian finite-strain EoS

$$K_S = K_{S0}(1 + 2f)^{5/2}\{1 + [3(\partial K_S/\partial P)_T - 5]f\},$$

$$G = (1 + 2f)^{5/2}\{[G_0 + (3K_{S0}(\partial G/\partial P)_T - 5G_0)]f\},$$

$$f = (1/2)[(V_0/V)^{2/3} - 1],$$

where  $(\partial K_S/\partial P)_T$  and  $(\partial G/\partial P)_T$  are the pressure derivative of the  $K_S$  and  $G$  at 298 K, respectively,  $f$  is the Eulerian strain, and  $V_0$  and  $V$  are unit-cell volume at ambient pressure and high pressure, respectively.<sup>26</sup> The derived  $K_S$  and  $(\partial K_S/\partial P)_T$  were further converted to the isotherm bulk modulus ( $K_T$ ) and its pressure derivative at constant temperature  $(\partial K_T/\partial P)_T$  using the following thermodynamic relations:

$$K_{T0} = K_{S0}/(1 + \alpha\gamma T),$$

$$(\partial K_T/\partial P)_T = (1 + \alpha\gamma T)^{-1}[(\partial K_S/\partial P)_T - (\gamma T/K_{T0})(\partial K_T/\partial T)_P],$$

where  $(\partial K_T/\partial T)_P$  is the temperature derivative of the  $K_T$  at constant pressure,  $K_{T0}$  is the isothermal bulk modulus at ambient conditions,  $\alpha$  is the thermal expansion coefficient, and  $\gamma$  is the Grüneisen parameter.<sup>27</sup> The temperature derivative of the bulk modulus  $(\partial K_T/\partial T)_P$  was calculated to be 0.0137

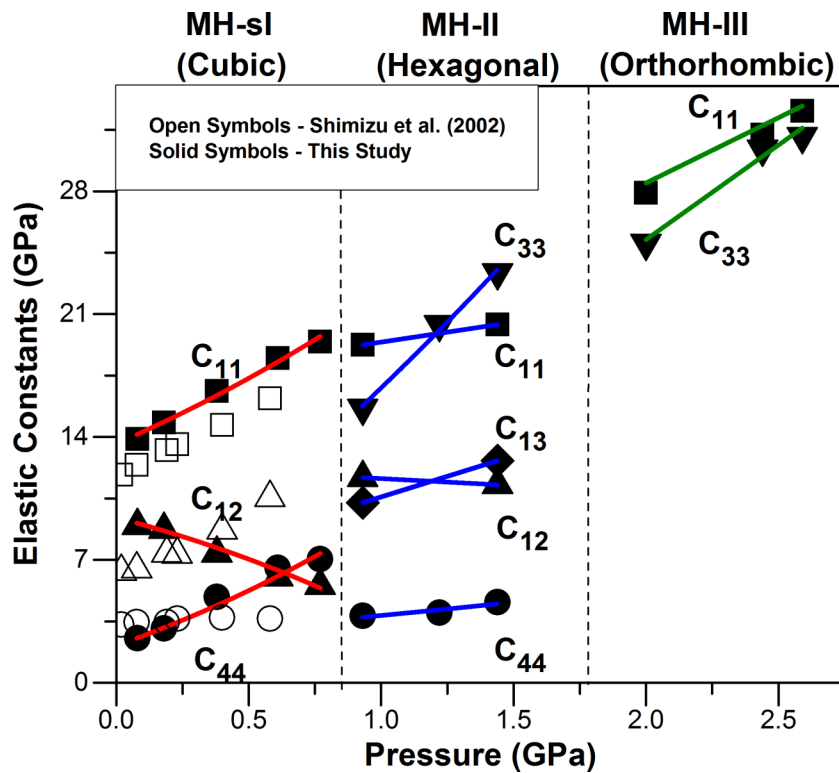


FIG. 7. Elastic constants for MH-sI, MH-II, and MH-III phases as a function of pressure at ambient temperature. Solid symbols are from this study. Open symbols are from Shimizu *et al.*<sup>12</sup> Only  $c_{11}$  and  $c_{33}$  are derived for MH-III, while the remaining  $c_{ijs}$  could not be calculated due to the lower symmetry of the crystal and the lack of observable  $V_S$  and  $V_P$  in only one confined crystal platelet in the DAC. Colored lines represent finite-strain fits to the experimental data for each phase.

( $\pm 0.0003$ ) and the pressure derivative of the bulk modulus ( $\partial K_s / \partial P$ )<sub>T</sub> was calculated to be  $-1.79 (\pm 0.03)$ . Those parameters along with the reported thermal expansion coefficient,<sup>15</sup>  $\alpha$ , of  $77 \times 10^{-6} \text{ K}^{-1}$ , the Grüneisen parameter,<sup>28</sup>  $\gamma$ , of 3.86, the calculated bulk and shear moduli, and the initially calculated elastic constants were used in iterations to calculate more accurate densities and thus elastic constants, shear and bulk moduli, and aggregate velocities for MH-sI until all parameters were self-consistent with the initial inputs (Figs. 7 and 8). The

anisotropy for MH-sI was then calculated using equations

$$A_P = 2 \times \frac{(V_{P,max} - V_{P,min})}{(V_{P,max} + V_{P,min})} \times 100\%,$$

$$A_S = \frac{(V_{S1} - V_{S2})}{V_S} \times 100\%,$$

resulting with a  $V_P$ , compressional wave velocity, anisotropy or  $A_P$  of 3.96% and a  $V_S$ , shear wave splitting velocity, anisotropy or  $A_S$  of 16.67% (Fig. 9).

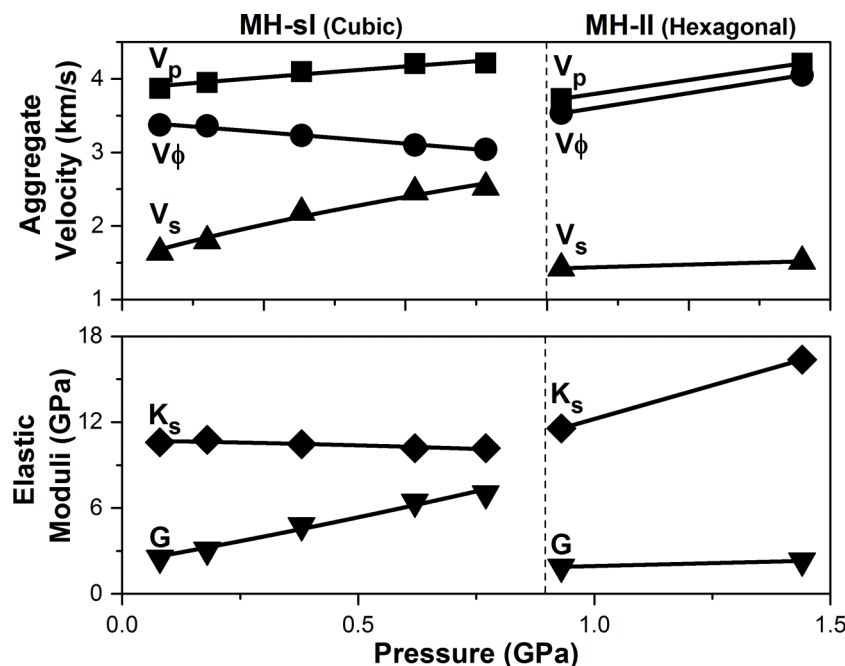


FIG. 8. Derived elastic moduli and aggregate velocities for MH-sI and MH-II phases at high pressures and ambient temperature. Panel (a): adiabatic bulk modulus ( $K_s$ ) and shear modulus ( $G$ ); panel (b): aggregate compressional wave velocity ( $V_P$ ), shear wave velocity ( $V_S$ ), and bulk sound velocity ( $V_\phi$ ).

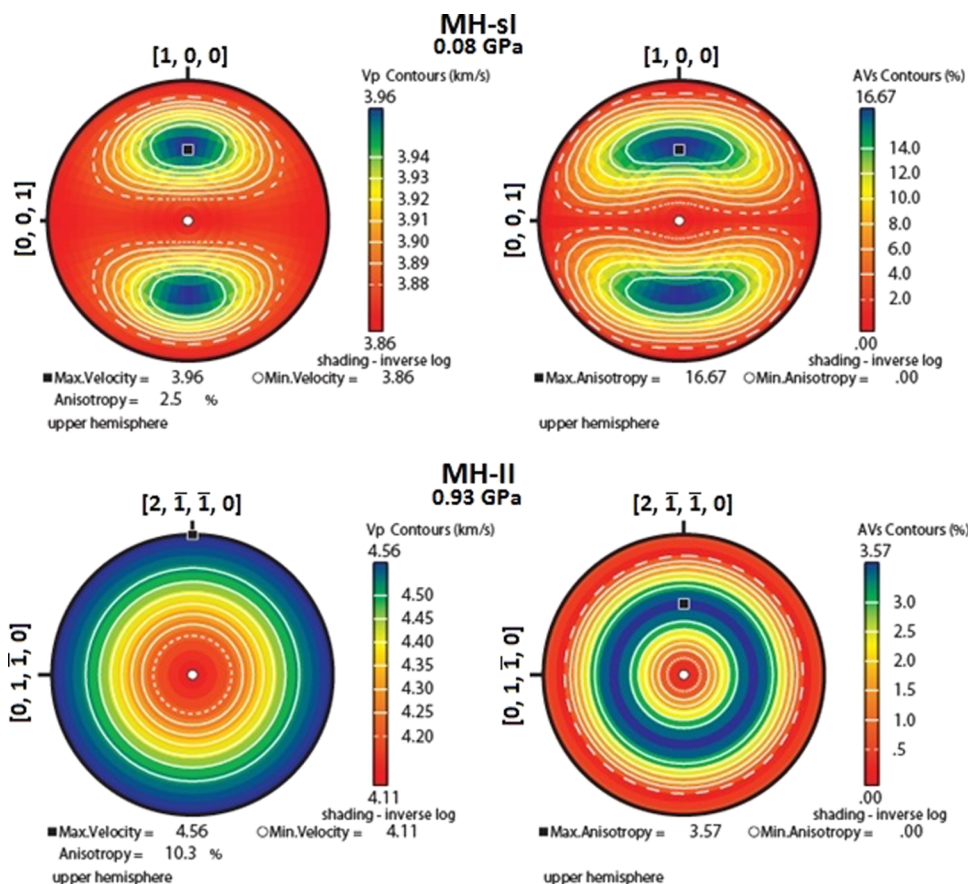


FIG. 9. Representative anisotropy patterns of compressional ( $V_P$ ) and transverse ( $V_S$ ) velocities for MH-sI at 0.08 GPa and MH-II at 0.93 GPa. MH-sI shows extremely strong anisotropies in the  $V_P$  and  $V_S$  velocities, whereas MH-II is almost elastically isotropic.

The five elastic constants,  $c_{11}$ ,  $c_{12}$ ,  $c_{13}$ ,  $c_{33}$ , and  $c_{44}$ , required to fully describe the elasticity of the hexagonal MH-II structure were derived using the measured  $V_P$  and  $V_S$  velocities as a function of the azimuthal angle at pressures between 0.93 GPa and 1.44 GPa (Figs. 6 and 7). Similar to the aforementioned modelling procedure for MH-sI phase, a finite strain theory was used to fit the stiffness as a function of pressure and the bulk and shear moduli. The aggregate bulk, shear, and compressional wave velocities were calculated from the stiffnesses and fit linearly (Fig. 8).  $c_{11}$  and  $c_{44}$  experience shifts to lower values across the phase transition from MH-sI to MH-II, and then, proceed to increase as pressure increases.  $c_{33}$  increases as pressure increases at a faster rate than  $c_{11}$  and even proceeds to cross  $c_{11}$ .  $c_{12}$  decreases as pressure increases, but at a lower rate.  $c_{13}$  with a positive correlation with pressure is initially lower than  $c_{12}$  but proceeds to cross  $c_{12}$ . The anisotropy for MH-II was then calculated resulting with a  $V_P$  anisotropy of 4.56% and a  $V_S$  anisotropy of 3.57% (Fig. 9).

There are nine elastic constants required to define the orthorhombic MH-III:  $c_{11}$ ,  $c_{12}$ ,  $c_{13}$ ,  $c_{22}$ ,  $c_{23}$ ,  $c_{33}$ ,  $c_{44}$ ,  $c_{55}$ , and  $c_{66}$ , but since the TA mode could not be detected, only  $c_{11}$  and  $c_{33}$  could be derived using our experimental results (Figs. 6 and 7).<sup>22</sup>  $c_{11}$  and  $c_{33}$  are dependent solely on the  $V_P$ , and therefore, could be calculated.<sup>22</sup> The bulk and shear moduli could not be calculated for the orthorhombic phase due to the incomplete stiffness set.  $c_{11}$  and  $c_{33}$  are very close together and both increase as pressure increases.

## IV. DISCUSSION

### A. EoS parameters and methane chemistry in MH phases

Comparison of the Raman spectroscopic results for MH-sI with that of Kumazaki *et al.*<sup>10</sup> and Sum *et al.*<sup>6</sup> shows that the C–H stretching modes of our results are consistent with literature values. As pressure increases from 0.08 GPa to 0.91 GPa, the large cages' Raman band only experiences a slight shift, whereas the shift to higher frequencies of the small cages' peak is more profound. Due to the consistency of these results, the chemistry of the MH-sI used for the density calculations was 7.67 methane molecules for every 46 water molecules based on 90% occupation of the small cages and 100% occupation of the medium cages, as reported by Sum *et al.*<sup>6</sup>

In MH-II, the Raman spectra show a single Raman band that de-convolves into two separate bands as pressure increases. The de-convolution of the single band is a major indicator for a phase change due to a chemistry and/or structural change. The first band at lower pressures is the overlapping of the Raman peaks from all three-cage types present in the phase. As pressure increases, a smaller band forms at a higher frequency corresponding to the large  $5^{12}6^8$  cage form.<sup>10</sup> The large  $5^{12}6^8$  cages have a much larger radius of 5.71 Å compared to that of the small cages and are therefore able to host more methane molecules; the small  $5^{12}$  and  $4^35^66^3$  cages' bands continuously overlap due to their very

similar average cage radii of 3.91 Å and 4.06 Å, respectively.<sup>10</sup> It has been reported that once all of the small cages are filled with a single methane molecule, the larger cage may take in an additional 2 or 3 guest gas molecules.<sup>10</sup> Recently, Tulk *et al.* found that the average cage occupancy of the large cages in MH-II is approximately 3.1 at 1.9 ( $\pm 0.2$ ) GPa, which is the upper end of the pressure stability for the phase.<sup>29</sup> The consistency of the frequency of the band created by all the small cages at high pressures indicates that no structural change has occurred. Therefore, the de-convolution of the single Raman band at higher pressures is due to a chemistry phase change as the large cage experiences an increase in the number of the housed methane molecules.<sup>10</sup> This chemistry difference of the increased methane to water ratio then acts as a major indicator of a reservoir's potential to produce a higher volume of methane gas. The chemistry before the phase transition used to calculate density was then estimated to be 5 methane molecules for every 34 water molecules based on Udachin *et al.*<sup>11</sup> who reported that the small cages were 80% occupied and the large cages were 100% occupied. After the chemistry change, the ratio between methane and water used for density calculations was 7 methane molecules for every 34 water molecules, because the chemistry shift indicates that there are now 2-3 methane molecules in the large cage and there is full occupation of the smaller cages.

The Raman spectra for MH-III consist of a single broad band that has a positive correlation with pressure and is consistent with results from Kumazaki *et al.*<sup>10</sup> There is a single band because of the lack of cages in this structure, and therefore, the chemistry for MH-III could not be estimated based upon the Raman spectra.

The EoS parameters of MH-sI and MH-III are consistent with the results from Loveday *et al.*;<sup>8</sup> however, our derived unit cell volume at a given pressure for MH-II was significantly lower. This discrepancy could be due to chemistry differences between this study and that of Loveday *et al.*<sup>8</sup> The structure of MH-sI of this study was confirmed to be cubic based on the consistency of the EoS and previously reported Miller Indices.<sup>6</sup> Despite the discrepancy for MH-II, our diffraction spectra and determination of the Miller indices and cell parameters, as well as the unique solutions for deriving elastic constants, support previous reports that the MH-II structure is indeed hexagonal. Due to the consistency of the XRD spectra for MH-III, the chemistry used to calculate the density of MH-III was 4 methane molecules for 8 water molecules reported by Loveday *et al.*<sup>8</sup> This consistency also supported the determined structure of MH-III as orthorhombic and allowed us to report Miller indices for the MH-III phase, which have not been reported before. The parameters for each phase along with each phase's estimated chemistry were then used to calculate more reliable densities, which in turn allowed for more accurate elastic constant calculations.

## B. Elasticity

For MH-sI, both the  $c_{11}$  and  $c_{44}$  increase with pressure, which is consistent with results from Shimizu *et al.*<sup>12</sup> However,  $c_{12}$  experiences a negative correlation with pressure, which is not consistent with the results of Shimizu *et al.*<sup>12</sup> The  $c_{11}$  trend

is parallel to that of Shimizu *et al.*,<sup>12</sup> but is slightly stiffer. The  $c_{44}$  trend in this study has a much steeper slope compared to that of the previous report.<sup>12</sup> The inconsistency between the studies is most likely due to differences in the chemistry of the clathrates.<sup>12</sup> The negative trend of the  $c_{12}$  also results in a slight negative correlation between the bulk modulus and pressure as well as for the aggregate bulk sound velocity and pressure. It is difficult to compare the derived elasticity directly with the chemistry of methane clathrate hydrates, but it is possible to discuss the bulk modulus for different phases. The shear modulus and the aggregate compressional velocity and shear velocity have a positive correlation with pressure. After the phase transition from MH-sI to MH-II,  $c_{44}$  experiences an approximate 45.9% decrease, and  $c_{12}$  experiences an approximate 110.1% increase while —  $c_{11}$  remains almost unaffected. The slopes of these three stiffnesses all become less steep in the hexagonal phase.

Huo *et al.*<sup>15</sup> reported the theoretical stiffness for the hexagonal phase at 0 K and ambient pressure having the stiffnesses  $c_{11}$ ,  $c_{12}$ ,  $c_{13}$ ,  $c_{33}$ , and  $c_{44}$ , as 15.9 GPa, 4.8 GPa, 5.7 GPa, 4.5 GPa, and 17.3 GPa, respectively. These results are only somewhat consistent with the results from this study.  $c_{11}$ ,  $c_{44}$ , and  $c_{12}$  experimental stiffnesses are consistent with the calculations; however,  $c_{33}$  is severely overestimated and  $c_{12}$  is underestimated. The theoretical results assume no temperature effect and full cage occupancy. As the Raman results of this and previous studies show, the cage occupancy changes as a function of pressure where the cages can contain 0, 1, or several guest molecules. The large deviation of the  $c_{12}$  and  $c_{33}$  stiffness can be attributed to the major chemistry change in the hexagonal crystal as pressure increases: there is an increase in the number of methane molecules in the large cage. Huo *et al.*<sup>15</sup> also pointed out that the temperature effects soften the stiffnesses. This discrepancy can contribute to the overestimation of the  $c_{33}$  but could not explain the underestimation of  $c_{12}$ . These discrepancies between the experimental and theoretical results and their causes indicate the enormous role the chemistry and subsequently the occupancy of the cages has on the stiffness, especially  $c_{12}$  and  $c_{33}$ , of methane clathrates. There is also a large increase in both of the shear and bulk moduli as a function of pressure relative to their counterparts for MH-I. The increase in the bulk modulus of the MH-II as a function of pressure indicates that MH-II is becoming increasingly incompressible at higher pressures. This decrease in compressibility could be due to the increase in the number of methane molecules in the large cages or the shortening of the C–H bonds in the methane molecules as pressure increases.<sup>12</sup> Tulk *et al.* also suggest that multiple methane molecules in a single cage repulsively react due to intermolecular potentials.<sup>29</sup> Thus, the change in the number of methane molecule would change the interactions within the cage. The positive relationship between the bulk modulus and pressure from this study thus supports the notion of the lattice stiffening for the MH-II phase due to changes in the cage occupancies. Overall, MH-I is more compressible than MH-II. The Kumazaki *et al.*<sup>10</sup> also report that the increase in the number of guest molecules in the large cages can only occur if the smaller cages are all occupied, which then requires that there be enough methane

in the surrounding environment. The elasticity can then be used as a major indicator of the chemistry, which can be an indicator of the abundance of methane gas in the MH reservoir environment and its subsequent potential as an energy source, as well as degree to which methane gas plays as a constituent on icy satellites. It would be worthwhile to closely analyze the elasticity of methane clathrates as a function of its chemistry in order to detect the amount of methane gas in a reservoir, which affects its potential as a hydrocarbon play.

As pressure increases and MH-II completes the phase transition to MH-III,  $c_{11}$  experiences a dramatic increase of 36.8%, and  $c_{33}$  experiences a subtler jump of 7.2%. The slope of  $c_{11}$  becomes shallower but maintains a positive correlation with pressure, while the slope of  $c_{33}$  gains a larger correlation with pressure. MH-III is an orthorhombic structure that requires 9 elastic constants to fully resolve its elasticity; however, the lack of  $V_S$  in the Brillouin spectra prevents the other 7 stiffnesses from being calculated.  $c_{11}$  and  $c_{33}$  are solely dependent on the  $V_P$ , whereas the other stiffnesses require information from solely  $V_S$  or from both velocities. The information from the  $V_P$  stiffnesses,  $c_{11}$  and  $c_{33}$ , indicates that the MH continues to become stiffer as pressure increases and across the phase transitions.

### C. Acoustic $V_P$ and $V_S$ anisotropies

MH-sI and MH-II phases have similar  $V_P$  anisotropy, 4.56% and 3.96%, respectively, but MH-sI is more anisotropic in the  $V_S$ , with 16.67% anisotropy, than the MH-II  $V_S$ , with 3.57% anisotropy. This may have important implications for using seismic waves to detect their potential presence and texturing. As seismic waves are directed into a medium, they will behave differently as they propagate through an anisotropic bed compared to an isotropic counterpart.<sup>22</sup> Anisotropic mediums cause the shear wave to split into a fast s-wave and a slow s-wave, while isotropic mediums do not cause any splitting.<sup>22</sup> The behavior of the seismic waves provides invaluable information regarding the anisotropy of the subsurface, allowing us to identify the phase. This is important as the phases have different potentials as hydrocarbon reservoirs, because the mole-to-mole ratio for methane to water is different within each phase. MH-II contains much more methane gas with 6 methane molecules for every 34 water molecules compared to MH-sI, which has a 8–46 methane to water ratio, and would therefore be more desirable for hydrocarbon ventures. This also has major implications for estimating the amount of MH that constitutes icy moons as it could provide information to estimate the amount of methane present and constraints on the temperature-pressure conditions of the moons. The relevance of these results is amplified due to the fact that the MH crystals are coexisting with water and/or ice, similar to realistic conditions on those of icy planetary moons. Large moons such as Titan and Ganymede have high pressures reaching upwards of ~1000 MPa and low temperatures that are capable of housing reservoirs of MH-sI and MH-II, and MH-III.<sup>30,31</sup> It has been proposed that Titan has a water cycle similar to that of Earth, where the water is actually methane and the cycle time scales are much larger.<sup>32</sup> The methane is proposed to be housed in

methane clathrate reservoirs in the subsurface of Titan, which release methane gas slowly into the atmosphere where the gas condenses and returns to the surface.<sup>30–32</sup> The anisotropy of the MH allows for real estimates into how much methane gas is present and therefore the extent of this methane-cycle on Titan. Low temperatures have similar effects as pressure on methane clathrates, and can produce high-pressure phases, so moons such as Enceladus, which does permit high pressures in its subsurface, can indeed house methane clathrates due to its low temperature conditions.<sup>33,34</sup> The exact temperature and pressure conditions on these satellites remain left to speculation and modeling; therefore, observations regarding the phase of the hydrates present could provide constraints on the pressure and temperature conditions. Thus, the full elastic constants and the derived velocity anisotropies may become crucial for determining the amount of methane gas present in the MH reservoirs and the pressure-temperature conditions on these icy satellites.

## V. CONCLUSIONS

Single-crystal MH-sI, MH-II, and MH-III were synthesized in a DAC at room temperature in order to investigate their elastic properties at high pressures. By using visual observations, *in situ* Raman measurements and X-ray diffraction measurements, we observed the phase transitions from MH-sI to MH-II at 0.93 GPa and from MH-II to MH-III at 2.0 GPa and the phase's respective general chemistry, EoS, and thus, densities. The structure of MH-II was confirmed as hexagonal supporting results from Loveday *et al.*,<sup>5</sup> and the Miller indices and their respective  $d$ -spacing for MH-III were calculated. The elastic constants, bulk and shear moduli, and the aggregate velocities were calculated using the estimated densities and Brillouin light scattering measurements. The elastic constants for MH-sI are not in agreement with results from Shimizu *et al.*,<sup>12</sup> nor are the elastic constants for MH-II in agreement with theoretical results from Huo *et al.*,<sup>15</sup> these discrepancies were discussed and attributed to chemistry differences in the MH. The two elastic constants,  $c_{11}$  and  $c_{33}$ , could only be calculated from MH-III due to the lack of  $V_S$  present, but demonstrate that stiffness does indeed continue to increase with increasing pressure.  $V_P$  and  $V_S$  anisotropies were calculated for MH-sI and MH-II and showed that MH-sI was much more anisotropic in the  $V_S$  than MH-II, while MH-sI and MH-II have similar  $V_P$  anisotropy. The bulk and shear moduli, as well as the aggregate velocities, were calculated for MH-sI and MH-II. These results provide — new insight into the determination of how much methane exists in MH reservoirs on Earth and on icy satellites elsewhere in the solar system and puts constraints on their environments' pressure and temperature conditions.

## ACKNOWLEDGMENTS

We acknowledge A. Nayak, A. Shulyak, E. Beam III, C. Tulk, N. Purevjav, and T. Okuchi for their constructive discussions. We also thank V. Prakapenka and Y.-Y. Chang for their assistance in the XRD experiments. J.-F.L. acknowledges financial support from the Extreme Physics

and Chemistry Program of the Deep Carbon Observatory and the Seed Grant of the Jackson School of Geosciences. J.B. acknowledges financial support from the Burke Undergraduate Research Fund of the Department of Geological Sciences at the University of Texas at Austin. The Brillouin system was partially funded by the Carnegie-DOE Alliance Center (CDAC) Program. Portions of this work were performed at GeoSoilEnviroCARS, Advanced Photon Source, Argonne National Laboratory. GSECARS was supported by the National Science Foundation (No. EAR-0622171) and Department of Energy (No. DE-FG02-94ER14466) under Contract No. DE-AC02-06CH11357. Portions of this work were performed at GeoSoilEnviroCARS, Advanced Photon Source, Argonne National Laboratory. GSECARS was supported by the National Science Foundation (No. EAR-0622171) and Department of Energy (No. DE-FG02-94ER14466) under Contract No. DE-AC02-06CH11357.

- <sup>1</sup>E. D. Sloan, *Nature (London)* **426**, 353 (2003).
- <sup>2</sup>J. L. Lunine and D. J. Stevenson, *Icarus* **70**, 67 (1987).
- <sup>3</sup>E. D. Sloan, *Clathrate Hydrates of Natural Gas*, 2nd ed. (Marcel Dekker, New York, 1998).
- <sup>4</sup>J. S. Tse, M. L. Klein, and I. R. McDonald, *J. Phys. Chem.* **87**, 4198 (1983).
- <sup>5</sup>J. S. Loveday, R. J. Nelmes, D. D. Klug, J. S. Tse, and S. Desgreniers, *Can. J. Phys.* **81**, 539 (2003).
- <sup>6</sup>A. K. Sum, R. C. Burruss, and E. D. Sloan, *J. Phys. Chem.* **101**, 7371 (1997).
- <sup>7</sup>H. Shimizu, T. Kumazaki, Y. Kume, and S. Sasaki, *J. Phys. Chem. B* **106**, 30 (2002).
- <sup>8</sup>J. S. Loveday, R. J. Nelmes, M. Guthrie, S. A. Belmonte, D. R. Allan, D. D. Klug, J. S. Tse, and Y. P. Handa, *Nature (London)* **410**, 661 (2001).
- <sup>9</sup>J. S. Loveday, R. J. Nelmes, M. Guthrie, D. D. Klug, and J. S. Tse, *Phys. Rev. Lett.* **87**, 21 (2001).
- <sup>10</sup>T. Kumazaki, Y. Kito, S. Sasaki, T. Kume, and H. Shimizu, *Chem. Phys. Lett.* **388**, 18 (2004).
- <sup>11</sup>K. A. Udachin, C. I. Ratcliffe, and J. A. Ripmeester, *J. Supramol. Chem.* **2**, 405 (2002).
- <sup>12</sup>H. Shimizu, T. Kumazaki, T. Kume, and S. Sasaki, *Phys. Rev. B* **65**, 212102 (2002).
- <sup>13</sup>H. Hirai, T. Tanaka, T. Kawamura, T. Yamamoto, and T. Yagi, *Phys. Rev. B.* **68**, 172102 (2003).
- <sup>14</sup>J. Shu, X. Chen, I. M. Chou, W. Yang, J. Hu, R. J. Hemley, and H. Mao, *Geosci. Front.* **2**(1), 93 (2011).
- <sup>15</sup>H. Huo, Y. Liu, S. Zheng, J. Zhao, C. Jin, and T. Lv, *J. Renewable Sustainable Energy* **3**, 063110 (2011).
- <sup>16</sup>H. K. Mao, J. Xu, and P. M. Bell, *J. Geophys. Res.* **91**, 4673, doi:10.1029/JB091iB05p04673 (1986).
- <sup>17</sup>A. P. Nayak, T. Pandev, D. Voiry, J. Liu, S. T. Moran, A. Sharma, C. Tan, C. H. Chen, L. J. Li, M. Chhowalla, J. F. Lin, A. Singh, and D. Akinwande, *Nano Lett.* **15**, 346 (2015).
- <sup>18</sup>C. Lu, Z. Mao, J. F. Lin, K. K. Zhuravlev, S. Tkachev, and V. B. Prakapenka, *Earth Planet. Sci. Lett.* **361**, 134 (2013).
- <sup>19</sup>M. Choukroun, Y. Morizet, and G. Olivier, *J. Raman Spectrosc.* **38**, 440 (2006).
- <sup>20</sup>A. Boultif and D. Louer, "Powder pattern indexing with the dichotomy method," *J. Appl. Cryst.* **37**, 724 (2004).
- <sup>21</sup>F. Birch, "Elasticity and constitution of the Earth's interior," *J. Geophys. Res.* **57**, 227, doi:10.1029/JZ057i002p00227 (1952).
- <sup>22</sup>G. Mavko, T. Mukerji, and J. Dvorkin, *The Rock Physics Handbook: Tools for Seismic Analysis of Porous Media* (Cambridge University Press, Cambridge, 2009).
- <sup>23</sup>A. Every, *Phys. Rev. B* **22**, 1746 (1980).
- <sup>24</sup>D. Mainprice, G. Barruol, and W. B. Ismail, *Geophys. Monogr.* **117**, 237 (2013).
- <sup>25</sup>R. Hill, *Proc. Phys. Soc., Sect. A* **65**, 349 (1952).
- <sup>26</sup>F. Birch, *J. Geophys. Res.* **83**, 1257, doi:10.1029/JB083iB03p01257 (1978).
- <sup>27</sup>J. P. Poirier, *Introduction to the Physics of the Earth's Interior* (Cambridge University Press, Cambridge, 2001).
- <sup>28</sup>V. P. Shpakov, J. J. Tse, C. A. Tulk, B. Kvamme, and V. R. Belosludov, *Chem. Phys. Lett.* **282**, 107 (1998).
- <sup>29</sup>C. A. Tulk, D. D. Klug, A. M. dos Santos, G. Karotis, M. Gunthrie, J. J. Molaison, and N. Pradhan, *J. Chem. Phys.* **136**, 054502 (2012).
- <sup>30</sup>M. Choukroun, O. Grasset, G. Tobie, and C. Sotin, *Icarus* **205**, 581 (2010).
- <sup>31</sup>M. G. Kivelson, K. K. Khurana, and M. Volwerk, *Icarus* **157**, 507 (2002).
- <sup>32</sup>S. K. Atreya, E. Y. Adams, H. B. Niemann, J. E. Demick-Montelara, T. C. Owen, M. Fulchignoni, F. Ferri, and E. H. Wilson, *Planet. Space Sci.* **54**, 1177 (2006).
- <sup>33</sup>S. W. Kieffer, X. Lu, C. M. Bethke, R. G. Spencer, S. Marshak, and A. Navrotsky, *Science* **314**, 1764 (2006).
- <sup>34</sup>J. H. Roberts, *Icarus* **258**, 54 (2015).